

See discussions, stats, and author profiles for this publication at: <https://www.researchgate.net/publication/276831835>

# Effect of Metal in $M_3(\text{btc})_2$ and $M_2(\text{dobdc})$ MOFs for $\text{O}_2/\text{N}_2$ Separations: A Combined Density Functional Theory and Experimental Study

ARTICLE in THE JOURNAL OF PHYSICAL CHEMISTRY C · MARCH 2015

Impact Factor: 4.77 · DOI: 10.1021/jp511789g

---

CITATION

1

---

READS

42

4 AUTHORS, INCLUDING:



[Marie V. Parkes](#)

Sandia National Laboratories

9 PUBLICATIONS 87 CITATIONS

SEE PROFILE

# Effect of Metal in $M_3(\text{btc})_2$ and $M_2(\text{dobdc})$ MOFs for $\text{O}_2/\text{N}_2$ Separations: A Combined Density Functional Theory and Experimental Study

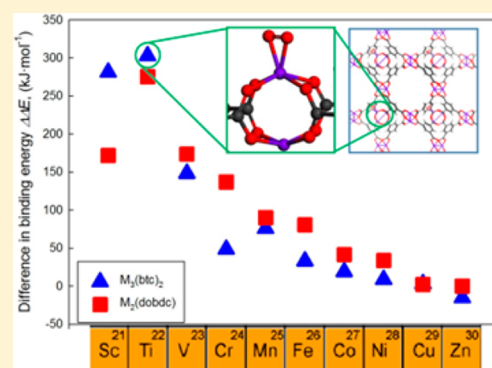
Marie V. Parkes,<sup>†</sup> Dorina F. Sava Gallis,<sup>‡</sup> Jeffery A. Greathouse,<sup>\*,†</sup> and Tina M. Nenoff<sup>\*,‡</sup>

<sup>†</sup>Geochemistry Department, Sandia National Laboratories, Albuquerque, New Mexico 87185-0754, United States

<sup>‡</sup>Nanoscale Sciences Department, Sandia National Laboratories, Albuquerque, New Mexico 87185-1415, United States

## S Supporting Information

**ABSTRACT:** Computational screening of metal–organic framework (MOF) materials for selective oxygen adsorption from air is used to identify new sorbents for oxyfuel combustion process feedstock streams. A comprehensive study on the effect of MOF metal chemistry on gas binding energies in two common but structurally disparate MOFs has been undertaken. Dispersion-corrected density functional theory (DFT) methods were used to calculate the oxygen and nitrogen binding energies with each of 14 metals, respectively, substituted into two MOF series,  $M_2(\text{dobdc})$  and  $M_3(\text{btc})_2$ . The accuracy of DFT methods was validated by comparing trends in binding energy with experimental gas sorption measurements. A periodic trend in oxygen binding energies was found, with greater oxygen binding energies for early transition-metal-substituted MOFs compared to late transition metal MOFs; this was independent of MOF structural type. The larger binding energies were associated with oxygen binding in a side-on configuration to the metal, with concomitant lengthening of the O–O bond. In contrast, nitrogen binding energies were similar across the transition metal series, regardless of both MOF structural type and metal identity. Taken together, these findings suggest that early transition metal MOFs are best suited to separating oxygen from nitrogen and that the MOF structural type is less important than the metal identity.



## 1. INTRODUCTION

Molecular oxygen is an important component in a number of industrial processes, including medical oxygen concentrators,<sup>1</sup> on-board oxygen generators for use in military airplanes,<sup>2–4</sup> and oxyacetylene welding.<sup>5</sup> Additionally, there has recently been interest in burning oxygen-enriched air (“oxyfuel”) in fossil-fuel power plants.<sup>6–8</sup> Oxyfuel combustion offers several advantages over air combustion: the furnace burns with higher flame temperature and therefore greater thermal efficiency; energy efficiency is increased because inert nitrogen is not heated in the furnace; flue gas volume is decreased by 75%;  $\text{NO}_x$  emissions are nearly eliminated due to a greatly reduced nitrogen presence in the combustion stream; and postcombustion carbon dioxide capture is simplified because the flue gas is more than 90% carbon dioxide.<sup>9</sup> In order to make oxyfuel combustion in power plants economically feasible, an energy-efficient and effective process for generating large amounts of relatively pure oxygen must be available.

Industrial-scale separation of oxygen from air is generally carried out by cryogenic separation, an energy-intensive process.<sup>10</sup> Cryogenic distillations can produce oxygen in very high purity, but require large facilities and expensive equipment.<sup>11</sup> Alternatives to cryogenic distillation include polymer membrane separation techniques and pressure-swing adsorp-

tion (PSA) employing porous materials, such as zeolites;<sup>10</sup> both are usually carried out on a smaller scale and result in lower final-purity separation ( $\sim 94\%$ ). Polymer membranes can be highly selective, but are not particularly permeable, requiring large membrane areas for an efficient separation.<sup>12</sup> PSA processes rely on the difference in kinetic selectivity of oxygen adsorption from other gases in air (primarily nitrogen).<sup>1,13–15</sup> The physical and chemical similarities of nitrogen and oxygen molecules make this process ineffective, and high-purity gas is difficult to produce. Currently, zeolites with nitrogen-to-oxygen selectivity ratios up to 14 are used in PSA processes.<sup>16</sup>

Metal–organic frameworks (MOFs) are porous, crystalline solids consisting of metal clusters connected by multidentate organic linkers forming a three-dimensional extended network. MOFs have found recent application in a wide variety of areas, including contaminant sensing,<sup>17,18</sup> luminescence,<sup>19–21</sup> catalysis,<sup>22,23</sup> nuclear waste remediation,<sup>24,25</sup> and drug delivery.<sup>26,27</sup> Because of their extremely high specific surface areas (up to  $6000 \text{ m}^2 \cdot \text{g}^{-1}$ ),<sup>28</sup> MOFs are able to adsorb and store great amounts of adsorbates.<sup>29–33</sup> MOFs have the potential to

Received: November 25, 2014

Revised: March 2, 2015

Published: March 2, 2015

replace zeolites in the PSA process, with performance and energy efficiency improvements due to better sorbent purity, fewer structural defects, and greater specific surface area relative to zeolites. Additionally, MOFs represent an improvement over zeolites in the separation of oxygen from air because MOFs can selectively adsorb oxygen (rather than nitrogen), resulting in the simultaneous separation of nitrogen and other air components from oxygen. Several MOFs have been used for small molecule gas separations based on either adsorptive or kinetic considerations.<sup>34–41</sup> The physical and chemical characteristics (including surface areas, framework topologies, pore diameters, surface chemistries, selectivities, and capacities) of MOFs can be tuned by carefully selecting the appropriate metal clusters and organic linkers through rational design.<sup>42,43</sup>

With thousands of reported MOF structures<sup>18,34</sup> and over 137000 hypothetical MOFs,<sup>44</sup> selecting the best MOF for a given application is difficult and time-consuming; experimentally testing each MOF is not feasible. Molecular modeling can efficiently identify the key molecular features of a group of MOFs and can be used for large-scale screening of both existing and hypothetical MOFs.<sup>34,44–49</sup>

Several MOFs are known to selectively bind oxygen over nitrogen at ambient temperatures, including those with  $[(\text{Co}_2(\text{bpbp}))_2(\text{bdc})](\text{PF}_6)_4$ ,<sup>50</sup>  $\text{Cr}_3(\text{btc})_2$ ,<sup>51</sup>  $\text{Fe}_2(\text{dobdc})$ ,<sup>7</sup>  $\text{Co}_4(\text{OH})_2(1,12\text{-dihydroxy-carbonyl-1,12-dicarba-closo-dodecaborane})_3$ ,<sup>52</sup> and  $\text{Co}(1,12\text{-dihydroxy-carbonyl-1,12-dicarba-closo-dodecaborane})_2(\text{pyridine})_2$ <sup>52</sup> and without (MOF-177,<sup>53</sup> UMCM-1<sup>54</sup>) coordinatively unsaturated metal sites. Two of these,  $\text{Cr}_3(\text{btc})_2$  and  $\text{Fe}_2(\text{dobdc})$ , are well-characterized MOFs with several known metal analogs.<sup>55–61</sup>

Although the frameworks  $\text{Cr}_3(\text{btc})_2$  (Figure 1) and  $\text{Fe}_2(\text{dobdc})$  (Figure 2) both have metals in the +2 oxidation

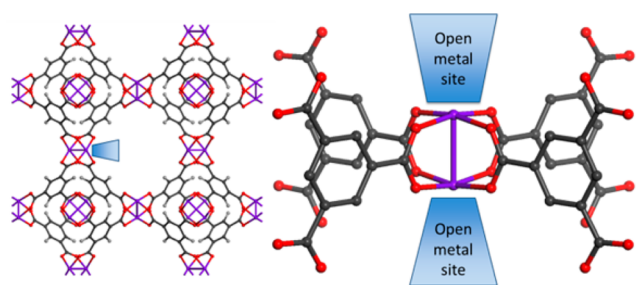


**Figure 1.**  $\text{Cr}_3(\text{btc})_2$  structure and binding site. Atoms are colored as follows: C, dark gray; O, red; Cr, purple. H atoms have been omitted for clarity.

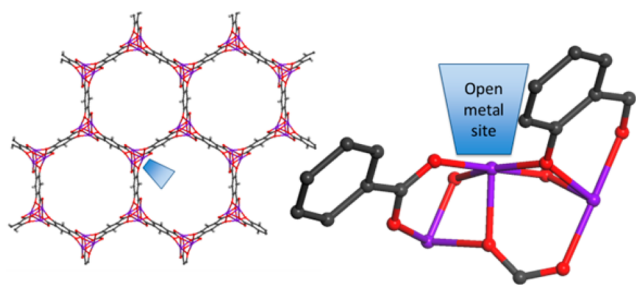


**Figure 2.**  $\text{Fe}_2(\text{dobdc})$  structure and binding site. Atoms are colored as follows: C, dark gray; O, red; Fe, purple. H atoms have been omitted for clarity.

state and both have coordinatively unsaturated metal sites, there are some key differences in the structures.  $\text{Cr}_3(\text{btc})_2$  has cages of void space approximately 7, 11, and 13 Å in diameter, connected to each other by windows approximately 4 and 7 Å wide.<sup>62</sup> In contrast,  $\text{Fe}_2(\text{dobdc})$  is characterized by one-dimensional pores approximately 10 Å in diameter spanning the length of the crystal parallel to the *c*-axis.<sup>63</sup> Chromium atoms in  $\text{Cr}_3(\text{btc})_2$  are clustered together in a dimetal paddlewheel configuration; iron atoms in  $\text{Fe}_2(\text{dobdc})$  are connected in infinite chains spanning the pores. The fact that both can effectively separate oxygen from nitrogen suggests that both metal electronic properties and framework structural properties play a role in oxygen/nitrogen separations.

Several studies have used quantum methods to estimate binding energies of small molecules on metal sites in MOFs. Snurr and co-workers used density functional theory (DFT) to predict trends in carbon dioxide binding to seven metal variants of  $\text{M}_2(\text{dobdc})$ , finding that DFT methods can qualitatively predict the order of binding energies for carbon dioxide adsorption among several MOFs in the  $\text{M}_2(\text{dobdc})$  series.<sup>64</sup> Yildirim and co-workers found that hydrogen adsorption on variants of  $\text{M}_2(\text{dobdc})$  depend strongly on the metal and that the general trend of the DFT-calculated binding energy agrees well with the trend seen experimentally.<sup>65</sup> Jung and co-workers examined carbon dioxide binding to  $\text{M}_2(\text{dobdc})$  variants that included the first row transition metal series and magnesium and calcium, finding that  $\text{Ti}_2(\text{dobdc})$  and  $\text{V}_2(\text{dobdc})$  have the strongest binding to carbon dioxide.<sup>66</sup> They attribute the particularly strong binding between carbon dioxide and  $\text{M}_2(\text{dobdc})$  ( $\text{M} = \text{Ti}, \text{V}$ ) to the ability of titanium and vanadium to accept donation of a lone pair of electrons from carbon dioxide into the metal's empty d-orbitals.

Two recent papers by Siegel and co-workers<sup>49,67</sup> examined the effect of DFT functional and dispersion correction method on binding energies of carbon dioxide on variants of  $\text{M}_2(\text{dobdc})$  and  $\text{M}_3(\text{btc})_2$ . They found that revPBE-vdW<sup>68</sup> predicted binding energies that had the best agreement with experimental enthalpies, but the metal–oxygen internuclear distances predicted by this method are significantly longer than experimental data. Although the DFT-D2 method slightly underpredicts experimental binding enthalpy,<sup>67</sup> the trend was consistent across four MOFs, and the metal–oxygen internuclear distances are only moderately overpredicted. Other studies report that the DFT-D2 method gives very good agreement with both experimental heats of adsorption<sup>69</sup> and high-level quantum calculations,<sup>30</sup> for carbon dioxide adsorption on  $\text{Mg}_2(\text{dobdc})$  and water adsorption on  $\text{Cu}_3(\text{btc})_2$ , respectively. Since the binding enthalpy is only slightly underpredicted and is consistent across several different MOFs, the selectivity obtained from DFT-D2 calculations should be reasonably accurate, making DFT-D2 a reasonable method to use to screen MOFs for binding energies.

Here, we build upon the previous computational work and use molecular modeling to identify the key features of MOFs that selectively adsorb oxygen over nitrogen. Two common MOF structures,  $\text{M}_3(\text{btc})_2$  and  $\text{M}_2(\text{dobdc})$ , were examined, with 14 metal variants of each MOF structure. In addition to the 10 first-row transition metals, the second-row transition metals Mo and Ru and the alkaline earth metals Be and Mg were examined. All metals were modeled in the +2 oxidation state. This set of metals allows us to probe the relative importance of the metal identity, identifying trends across the transition metal series from early transition metals to late

transition metals. The two second-row transition metals Mo and Ru were chosen because they are in the same group as Cr and Fe, which have been shown to effectively bind oxygen over nitrogen in the native structures  $\text{Cr}_3(\text{btc})_2$  and  $\text{Fe}_2(\text{dobdc})$ ,<sup>7,51</sup> to assess the importance of metal size and polarizability on the separation. Finally, Be and Mg were included to compare alkaline earth metals with transition metals in separating oxygen from nitrogen.

These 14 metals were substituted into each of the two framework structure types ( $\text{M}_3(\text{btc})_2$  and  $\text{M}_2(\text{dobdc})$ ) in order to examine the effect of metal properties on oxygen and nitrogen adsorption. Computational results are compared with experimental gas sorption studies to verify the accuracy of the DFT methods. Findings from these calculations are used to predict other MOFs that could more effectively separate oxygen and nitrogen under mild conditions. With a strong combination of modeling and experimental studies, this study shows the methodology for designing high selective MOFs for selective light gas sorption applications.

## 2. METHODS

**2.1. DFT: Initial Structures.** To probe the relative importance of MOF structure and metal character on oxygen/nitrogen adsorptive separations, we have performed binding energy calculations using dispersion-corrected DFT methods on a series of 28 MOFs.

Initial structures for known  $\text{Fe}_3(\text{btc})_2$ ,<sup>55</sup>  $\text{Cu}_3(\text{btc})_2$ ,<sup>56</sup>  $\text{Fe}_2(\text{dobdc})$ ,<sup>57</sup>  $\text{Co}_2(\text{dobdc})$ ,<sup>58</sup>  $\text{Ni}_2(\text{dobdc})$ ,<sup>59</sup>  $\text{Zn}_2(\text{dobdc})$ ,<sup>60</sup> and  $\text{Mg}_2(\text{dobdc})$ <sup>61</sup> materials were taken from published crystal structures, with solvent and coordinating water molecules removed and hydrogen atoms added, where necessary. All other hypothetical  $\text{M}_3(\text{btc})_2$  and  $\text{M}_2(\text{dobdc})$  frameworks were prepared by substituting the metals in representative model compounds  $\text{Fe}_3(\text{btc})_2$  and  $\text{Ni}_2(\text{dobdc})$  with the remaining metals. All structures were reduced to their primitive cells for calculations;  $\text{M}_3(\text{btc})_2$  and  $\text{M}_2(\text{dobdc})$  empty frameworks contained 156 and 54 atoms, respectively.

Initial structures for gaseous  $\text{O}_2$  and  $\text{N}_2$  were prepared as diatomic molecules with interatomic distances 1.21 and 1.24 Å, respectively, placed in a rectangular prism with sides 10 Å × 11 Å × 12 Å long.  $\text{O}_2$ - and  $\text{N}_2$ -containing MOFs were prepared by adding one molecule of oxygen or nitrogen into the fully optimized MOF framework, with the proximal gas atom approximately 2.0 Å from a metal center and O–O and N–N interatomic distances approximately 1.2 Å. Two initial structures, differing in the bonding geometry of the gas, were used for each gas-containing MOF. Preliminary structural models of MOFs containing oxygen were prepared in both side-on bonded (M–O–O angle, 67°) and bent (M–O–O angle, 120°) geometries; initial structures of MOFs containing nitrogen were prepared in both bent (120°) and linear (179°) geometries. See, for example, the optimized structures in Figures 3–5.

**2.2. DFT: Geometry Optimizations and Energy Calculations.** Plane wave DFT calculations were performed on periodic structures in the Vienna Ab Initio Simulation Package (VASP), version 5.2.12,<sup>70</sup> with the Perdew–Burke–Ernzerhof (PBE) functional,<sup>71,72</sup> including dispersion corrections (DFT-D2).<sup>73</sup> Although doubly hybrid functionals<sup>74</sup> could be used to better predict binding energies, the cost and availability of those calculations goes beyond the large screening set studied here.

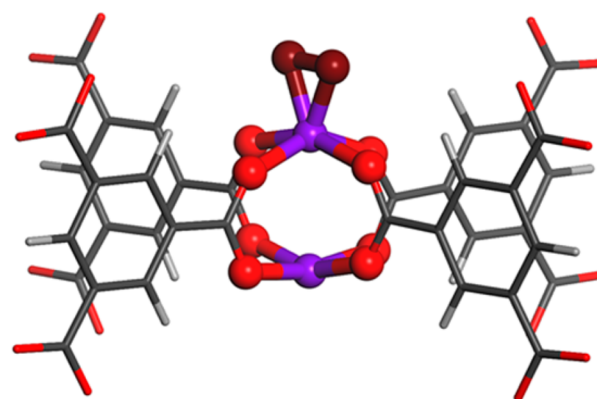


**Figure 3.** Side-on  $\text{O}_2$  binding to  $\text{V}_3(\text{btc})_2$ . Atoms are colored as follows: C, dark gray; H, light gray; framework O, red; V, purple; molecular  $\text{O}_2$ , dark red.

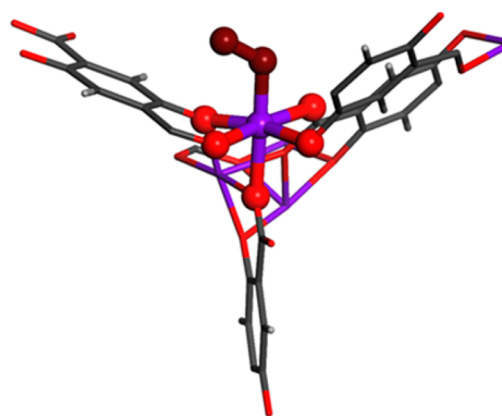


**Figure 4.** Bent  $\text{O}_2$  binding to  $\text{Co}_2(\text{dobdc})$ . Atoms are colored as follows: C, dark gray; H, light gray; framework O, red; Co, purple; molecular  $\text{O}_2$ , dark red.

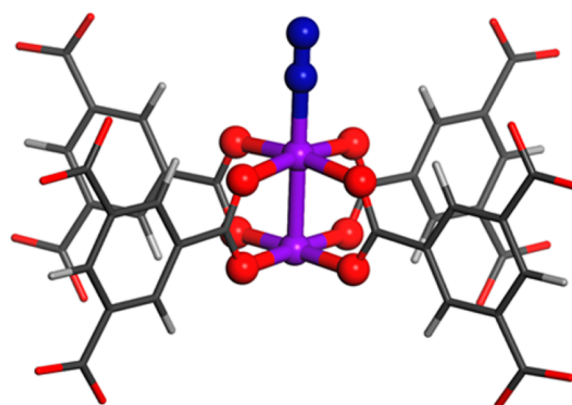


**Figure 5.** Linear  $\text{N}_2$  binding to  $\text{Ni}_3(\text{btc})_2$ . Atoms are colored as follows: C, dark gray; H, light gray; framework O, red; Ni, purple; N, blue.

All calculations were spin-polarized, with an initial magnetic moment on each atom equal to 1.0. This setting proved sufficient for convergence to reasonable structures and spin states for all systems except manganese-containing systems, for which the initial magnetic moment on manganese atoms was set to 4.5. The  $2 \times 2 \times 2$   $k$ -point meshes centered at the  $\Gamma$ -point were used to sample the Brillouin zone. Partial-occupancy smearing was done using the Methfessel–Paxton method of



order 1, with smearing width 0.2 eV. Atomic positions were relaxed using a conjugate-gradient algorithm with scaling constant 0.5. Electronic convergence was met when the total energy difference between two consecutive steps was smaller than  $10^{-4}$  eV; ionic convergence was met when all forces were smaller than 0.03 eV/Å. Core and valence electron interactions were described by the projector augmented-wave (PAW) formalism.<sup>75,76</sup> This method has been used previously to investigate trends in guest binding in MOFs with coordinatively unsaturated metal sites.<sup>30,49,77,78</sup>

For MOFs without added gas molecules, the geometry optimizations were completed in four successive steps, with final atomic positions, charge densities, and wave functions from each step used as input for subsequent steps:

- Step 1. Atomic positions relaxed, plane wave energy cutoff set to 500 eV, projected wave function evaluated in real space, and real space operators optimized to an accuracy of 0.5 eV/atom.
- Step 2. Atomic positions relaxed, cell volume relaxed anisotropically, plane wave energy cutoff set to 650 eV, projected wave function evaluated in real space, and real space operators optimized to an accuracy of 0.25 eV/atom.
- Step 3. Atomic positions relaxed, plane wave energy cutoff set to 500 eV, projected wave function evaluated in real space, and real space operators optimized to an accuracy of 0.25 eV/atom.
- Step 4. Atomic positions relaxed, plane wave energy cutoff set to 500 eV, projected wave function evaluated in reciprocal space, and real space operators optimized to an accuracy of 0.25 eV/atom.

Geometry optimizations of MOFs with oxygen or nitrogen were similar, except that the cell volume was not optimized (step 2 omitted). For geometry optimizations of O<sub>2</sub> or N<sub>2</sub> in empty boxes, only steps 3 and 4 were performed. Lattice parameters and space groups for the conventional unit cell optimized geometries are shown in Table S1, Supporting Information.

**2.3. DFT: Calculation of Binding Energies.** Static binding energies for oxygen and nitrogen at 0 K ( $\Delta E_{\text{gas}}$ ) were calculated by  $\Delta E_{\text{gas}} = \Delta E_{\text{MOF+gas}} - \Delta E_{\text{MOF}} - \Delta E_{\text{gas}}$  for gas = O<sub>2</sub> or N<sub>2</sub>, where  $E$  is the total energy of the system. The difference in binding energies ( $\Delta\Delta E$ ) for oxygen and nitrogen was calculated by  $\Delta\Delta E = -(\Delta E_{\text{O}_2} - \Delta E_{\text{N}_2})$ .

**2.4. Experimental Syntheses.** All materials were purchased from commercially available sources and used without further purification. Cu<sub>3</sub>(btc)<sub>2</sub> powder was purchased from Sigma-Aldrich under the commercial name of Basolite C300.

**Synthesis of Co<sub>2</sub>(dobdc).** The synthesis conditions were slightly modified from the procedure reported in the literature procedure.<sup>79</sup> The mixture of Co(NO<sub>3</sub>)<sub>2</sub>·6H<sub>2</sub>O (1.885g, 6.5 mmol) and 2,5-dihydroxyterephthalic acid (DOBDC, 0.24 g, 1.2 mmol) in a solution of DMF (33 mL), EtOH (33 mL), and H<sub>2</sub>O (33 mL) was placed in a convection oven at 100 °C for 1 day.

**Synthesis of Ni<sub>2</sub>(dobdc).** The synthesis conditions were slightly modified from the procedure reported in the literature procedure.<sup>79</sup> The mixture of Ni(NO<sub>3</sub>)<sub>2</sub>·6H<sub>2</sub>O (1.189g, 4 mmol) and 2,5-dihydroxyterephthalic acid (DOBDC, 0.24g, 1.2 mmol) in a solution of DMF (33 mL), EtOH (33 mL), and

H<sub>2</sub>O (33 mL) was placed in a convection oven at 100 °C for 3 days.

**2.5. Experimental X-ray Data Collection.** Powder X-ray diffraction (XRD) measurements were performed on a Siemens Kristalloflex D500 diffractometer, Cu K $\alpha$  radiation ( $\lambda$  = 1.54178 Å). The structural integrity of the framework was maintained after gas adsorption, as seen by powder X-ray diffraction, confirming that the material was not destroyed in the process of gas adsorption (Figures S2–S4). The identity and purity of each sample was confirmed by the good correlation between the calculated and synthesized powder XRD patterns (Figures S2–S4).

**2.6. Experimental Sample Activation and Gas Adsorption Measurements.** Commercial samples of Cu<sub>3</sub>(btc)<sub>2</sub> were activated under dynamic vacuum at 180 °C for 6 h. The as-synthesized Co<sub>2</sub>(dobdc) and Ni<sub>2</sub>(dobdc) samples were washed 3 times with 15 mL of hot DMF, followed by washing with 15 mL of hot MeOH. Samples were further soaked in MeOH for 3 days, (replenished with fresh solvent every 24 h). Further, the samples were activated under vacuum at 180 °C for 24 h. The Langmuir surface areas were calculated using the nitrogen adsorption isotherm measured at 77 K (Figure S1). Measured Langmuir surface areas were 2141 m<sup>2</sup>/g (Cu<sub>3</sub>(btc)<sub>2</sub>), 1417 m<sup>2</sup>/g (Co<sub>2</sub>(dobdc)), 1234 m<sup>2</sup>/g (Ni<sub>2</sub>(dobdc)); these results are in good agreement with the highest values reported in previously published data,<sup>80,81</sup> inferring optimal sample activation.

Gas adsorption isotherms were measured using a Micromeritics ASAP 2020 surface area and porosity analyzer. Nitrogen and oxygen of ultrahigh purity 99.999% (Matheson Tri-Gas) were used in these experiments. Single-gas oxygen and nitrogen uptake were measured at 77 K up to 0.20  $P/P_0$ ; gas uptake at 0.015  $P/P_0$  was chosen as the lowest adsorption pressure in order to infer the strongest metal–gas interactions for the comparison with the binding energy calculations.

### 3. RESULTS AND DISCUSSION

In order to understand the key features of MOFs that selectively adsorb oxygen over nitrogen, metal-substituted variants of two MOFs that are known to selectively bind oxygen over nitrogen at ambient temperatures (Cr<sub>3</sub>(btc)<sub>2</sub> and Fe<sub>2</sub>(dobdc)) were examined computationally and compared to experimental adsorption isotherm data.

**3.1. DFT: Optimized Geometries.** Initially, DFT optimization of empty frameworks was performed. Lattice parameters were compared with crystal structures where available. The simulated cell lengths and angles are in strong agreement with the published crystal structure lattice parameters, within 5%, as shown in Table 1.

For each MOF–gas complex, the gas molecule was initially placed near the metal center, in either a side-on bonded (oxygen only), bent (oxygen and nitrogen), or linear (nitrogen only) orientation. In many cases, the two initial structures optimized to geometries that were identical or nearly identical. For cases in which the two initial structures optimized to different geometries, the lower energy geometry was used as the optimized geometry.

For each [MOF + gas] optimized structure, the internuclear distance between the metal atom and the proximal gas atom was measured; see Tables 2–5. The internuclear distance was compared with all structures with M–O or M–N bonds in the Cambridge Structural Database (CSD).<sup>82–85</sup> Structures with internuclear distances within three standard deviations of the

**Table 1.** Lattice Parameters for DFT-Optimized MOF Structures, Compared with Experimental Values

MOF	DFT-optimized structure		crystal structure		ref.
	$a = b = c$ (Å)	$\alpha = \beta = \gamma$ (°)	$a = b = c$ (Å)	$\alpha = \beta = \gamma$ (°)	
Fe <sub>3</sub> (btc) <sub>2</sub>	26.3017	90.000	26.6328	90.000	55
Cu <sub>3</sub> (btc) <sub>2</sub>	26.4270	90.000	26.3430	90.000	56
	$a = b; c$ (Å)	$\alpha = \beta; \gamma$ (deg)	$a = b; c$ (Å)	$\alpha = \beta; \gamma$ (deg)	
Fe <sub>2</sub> (dobdc)	26.1633; 6.64888	90.000; 120.000	26.0468; 6.82816	90.000; 120.000	57
Co <sub>2</sub> (dobdc)	26.1633; 6.64888	90.000; 120.000	26.1579; 6.71822	90.000; 120.000	58
Ni <sub>2</sub> (dobdc)	25.5797; 6.73467	90.000; 120.000	25.7856; 6.77010	90.000; 120.000	59
Zn <sub>2</sub> (dobdc)	26.0000; 6.66414	90.000; 120.000	26.2205; 6.32019	90.000; 120.000	60
Mg <sub>2</sub> (dobdc)	26.0277; 6.77555	90.000; 120.000	26.0261; 6.75872	90.000; 120.000	61

mean M–O(N) distances were classified as bonded structures; those with internuclear distances greater than the maximum M–O(N) distances were classified as nonbonded. Five [MOF + N<sub>2</sub>] complexes and one [MOF + O<sub>2</sub>] complex had M–O(N) internuclear distances that were greater than three standard deviations of the mean M–O(N) distance but less than the maximum M–O(N) distance; those structures were examined individually to determine whether the internuclear distance was consistent with a bonded or nonbonded structure. All complexes that were classified as nonbonded are indicated in Tables 2–5 as (nb). Of the structures that formed bonded complexes with oxygen or nitrogen, roughly two-thirds of the O<sub>2</sub>-bound complexes and half of the N<sub>2</sub>-bound complexes had M–O(N) bonds that were shorter than the average M–O(N) bond found in the CSD, indicating a relatively strong bond.

Notably, only two [MOF + O<sub>2</sub>] complexes were found to be nonbonded: Be<sub>3</sub>(btc)<sub>2</sub> and Be<sub>2</sub>(dobdc). The nonbonded interaction between oxygen and the metal atoms can be explained by considering that beryllium is already bound to four

framework oxygen atoms in each structure. Four-coordinate beryllium has no empty orbitals and therefore is not able to form a bond with the oxygen molecule.

In contrast, there are five [MOF + N<sub>2</sub>] complexes that do not form M–N<sub>2</sub> bonds. These nonbonded [MOF + N<sub>2</sub>] structures represent a variety of metal atoms (Cr, Cu, Mo, and Be) and both M<sub>3</sub>(btc)<sub>2</sub> and M<sub>2</sub>(dobdc) structure types. Taken together, these results suggest that oxygen generally forms a stronger bond to the coordinatively unsaturated metal site than nitrogen does. This result supports our claim that MOFs with coordinatively unsaturated metal centers should be considered for the separation of oxygen from nitrogen.

All three gas bonding modes were identified based on the M–O–O (M–N–N) angles: side-on, bent, and linear bonding, with examples of each shown in Figures 3–5.

[MOF + O<sub>2</sub>]. These complexes exhibit either side-on or bent oxygen bonding depending on the metal. Molecular oxygen can bond in a side-on,  $\eta^2$  fashion (M–O–O angle 67–71°) to Sc-, Ti-, V-, Cr-, Mn-, and Fe-containing MOFs as well as to MOFs containing second-row transition metals (Mo and Ru). Side-on bonding is generally associated with stronger binding energies (generally  $\geq 100$  kJ·mol<sup>−1</sup>) than bent bonding (generally  $< 100$  kJ·mol<sup>−1</sup>), as discussed below.

Because both oxygen atoms coordinate to the metal atom, side-on bonding occurs exclusively with early transition metals, which have available d-orbitals that can accept electrons from the oxygen atoms. This side-on bonding may be preferred in complexes with empty metal d-orbitals because the oxygen HOMO bond is an antibonding  $\pi$  bond, which is perfectly oriented to interact with an empty metal d-orbital. In addition to this strong M–O binding energy, the O–O bond is weakened in side-on bonding, as evidenced by the slightly longer O–O bond in [MOF + O<sub>2</sub>] complexes with side-on bonding compared to those with bent bonding.

Notably, 3d M<sub>3</sub>(btc)<sub>2</sub> complexes that exhibit side-on bonding with oxygen undergo significant deformation at the metal binding site, in which the pseudoplane formed by the metal atom and four oxygen atoms deviates significantly from

**Table 2.** Binding Energies and Geometries of Oxygen Binding to M<sub>3</sub>(btc)<sub>2</sub> Variants

metal (M)	bonding mode <sup>a</sup>	binding energy (kJ·mol <sup>−1</sup> )	M–O distance <sup>b</sup> (Å)	O–O distance (Å)	M–O–O angle (°)
First-Row Transition Metals					
Sc	side-on	−328	1.94	1.47	68
Ti	side-on	−329	1.85	1.46	67
V	side-on	−158	1.82	1.45	67
Cr	bent	−100	1.84	1.28	135
Mn	bent	−264	1.87	1.28	126
Fe	bent	−45	1.99	1.29	118
Co	bent	−81	1.93	1.27	125
Ni	bent	−53	1.95	1.26	118
Cu	bent	−103	2.36	1.24	119
Zn	bent	−22	2.29	1.24	120
Second-Row Transition Metals					
Mo	bent	−18	2.50	1.26	119
Ru	side-on	−105	2.09	1.34	71
Alkaline Earth Metals					
Be	(bent)	−421	3.01 (nb)	1.23	115
Mg	bent	−218	2.32	1.23	122

<sup>a</sup>Side-on bonding mode corresponds to M–O–O angle 67–73°; Bent bonding mode corresponds to M–O–O angle 103–159°; Linear bonding mode corresponds to M–O–O angle 165–179°. <sup>b</sup>(nb) indicates that the metal–oxygen interatomic distance is too long to represent a bonding interaction.

Table 3. Binding Energies and Geometries of Oxygen Binding to  $M_2(\text{dobdc})$  Variants

metal (M)	bonding mode <sup>a</sup>	binding energy (kJ·mol <sup>-1</sup> )	M–O distance <sup>b</sup> (Å)	O–O distance (Å)	M–O–O angle (°)
First-Row Transition Metals					
Sc	side-on	–215	1.93	1.46	69
Ti	side-on	–354	1.85	1.46	67
V	side-on	–264	1.82	1.41	71
Cr	side-on	–147	1.83	1.42	68
Mn	side-on	–116	1.86	1.40	68
Fe	side-on	–88	1.89	1.39	69
Co	bent	–83	1.84	1.29	118
Ni	bent	–79	1.88	1.27	117
Cu	bent	–31	2.37	1.25	118
Zn	bent	–21	2.35	1.25	118
Second-Row Transition Metals					
Mo	side-on	–267	1.96	1.44	70
Ru	bent	–157	1.91	1.31	117
Alkaline Earth Metals					
Be	(bent)	–14	3.20 (nb)	1.24	106
Mg	bent	–34	2.23	1.26	121

<sup>a</sup>Side-on bonding mode corresponds to M–O–O angle 67–73°; Bent bonding mode corresponds to M–O–O angle 103–159°; Linear bonding mode corresponds to M–O–O angle 165–179°. <sup>b</sup>(nb) indicates that the metal–oxygen interatomic distance is too long to represent a bonding interaction.

Table 4. Binding Energies and Geometries of Nitrogen Binding to  $M_3(\text{btc})_2$  Variants

metal (M)	bonding mode <sup>a</sup>	binding energy (kJ·mol <sup>-1</sup> )	M–N distance <sup>b</sup> (Å)	N–N distance (Å)	M–N–N angle (°)
First-Row Transition Metals					
Sc	bent	–46	2.31	1.14	148
Ti	bent	–26	2.35	1.13	136
V	linear	–10	2.28	1.12	168
Cr	(bent)	–52	2.80 (nb)	1.11	147
Mn	bent	–188	2.46	1.11	159
Fe	bent	–12	2.48	1.12	130
Co	linear	–62	1.95	1.12	177
Ni	linear	–44	1.98	1.12	179
Cu	linear	–100	2.36	1.11	174
Zn	linear	–38	2.21	1.11	178
Second-Row Transition Metals					
Mo	(bent)	–14	3.07 (nb)	1.11	135
Ru	linear	–55	2.07	1.13	179
Alkaline Earth Metals					
Be	(linear)	–424	2.86 (nb)	1.11	165
Mg	linear	–228	2.30	1.11	176

<sup>a</sup>Side-on bonding mode corresponds to M–O–O angle 67–73°; Bent bonding mode corresponds to M–O–O angle 103–159°; Linear bonding mode corresponds to M–O–O angle 165–179°. <sup>b</sup>(nb) indicates that the metal–oxygen interatomic distance is too long to represent a bonding interaction.

planarity. This can be clearly seen in Figure 3 with oxygen binding to  $V_3(\text{btc})_2$ , where the vanadium atom and four framework oxygen atoms are no longer coplanar after adsorption of oxygen in a side-on bonding mode. Quantitatively, the amount of deformation around the metal binding site can be calculated by

$$\frac{\angle \text{OMO}_{\text{trans}}^{\text{framework}} - \angle \text{OMO}_{\text{trans}}^{\text{[MOF+O}_2\text{]}}}{\angle \text{OMO}_{\text{trans}}^{\text{framework}}}$$

where  $\angle \text{OMO}_{\text{trans}}$  is the angle defined by the metal atom and two trans framework oxygen atoms. The three  $[\text{MOF} + \text{O}_2]$  complexes that exhibit side-on bonding have 15% ( $\text{Sc}_3(\text{btc})_2$ ), 11% ( $\text{Ti}_3(\text{btc})_2$ ), and 16% ( $\text{V}_3(\text{btc})_2$ ) deformation around the metal atom;  $[\text{MOF} + \text{O}_2]$  and  $[\text{MOF} + \text{N}_2]$  complexes that exhibit bent or linear bonding have less than 4% deformation.

Additional energetic and orbital-occupancy details of the bound complexes would be insightful but cannot be obtained from the planewave-based DFT calculation used here.

For MOF structures that optimized to both a side-on bonded oxygen structure and a bent oxygen structure, the side-on bonded structure was always lower in energy and the difference in energies was largest for early transition metals ( $\geq 40 \text{ kJ}\cdot\text{mol}^{-1}$  for Ti and V; 1.4–32  $\text{kJ}\cdot\text{mol}^{-1}$  for Cr, Mn, Fe, and Ru).

$[\text{MOF} + \text{N}_2]$ . Unlike oxygen, nitrogen bonding modes are generally independent of metal type or available d-orbitals. Nitrogen exhibits primarily linear bonding to the metal, although seven  $[\text{MOF} + \text{N}_2]$  structures optimized to a bent bonding mode for nitrogen. The bent  $[\text{MOF} + \text{N}_2]$  complexes are primarily of the type  $M_3(\text{btc})_2$  and generally occur early in the transition metal series. Several  $[\text{MOF} + \text{N}_2]$  structures optimized to both linear and bent bonding modes; the

Table 5. Binding Energies and Geometries of Nitrogen Binding to  $M_2(\text{dobdc})$  Variants

metal (M)	bonding mode <sup>a</sup>	binding energy (kJ·mol <sup>-1</sup> )	M–N distance <sup>b</sup> (Å)	N–N distance (Å)	M–N–N angle (°)
First-Row Transition Metals					
Sc	linear	−43	2.38	1.12	169
Ti	linear	−79	2.04	1.14	173
V	linear	−90	1.98	1.13	176
Cr	linear	−10	1.90	1.13	179
Mn	bent	−26	2.37	1.12	138
Fe	linear	−7	1.99	1.13	169
Co	linear	−41	1.94	1.12	177
Ni	linear	−46	2.00	1.12	171
Cu	(bent)	−29	2.92 (nb)	1.11	154
Zn	linear	−21	2.63	1.11	175
Second-Row Transition Metals					
Mo	linear	−128	2.00	1.14	179
Ru	linear	−131	1.87	1.14	178
Alkaline Earth Metals					
Be	(bent)	−15	3.38 (nb)	1.11	103
Mg	linear	−31	2.40	1.11	177

<sup>a</sup>Side-on bonding mode corresponds to M–O–O angle 67–73°; Bent bonding mode corresponds to M–O–O angle 103–159°; Linear bonding mode corresponds to M–O–O angle 165–179°. <sup>b</sup>(nb) indicates that the metal–oxygen interatomic distance is too long to represent a bonding interaction.

differences between these local minimum energy structures were generally small ( $\leq 7$  kJ·mol<sup>-1</sup>), indicating that nitrogen bent and linear bonding are very similar in energy for all metals. The case of nitrogen adsorption in  $\text{Cr}_2(\text{dobdc})$  initially drew our attention because it appears to represent a complex with a short Cr–N internuclear distance but a relatively weak bonding interaction. Upon closer examination, however, the 1.90 Å bond length is not particularly short for Cr–N bonds, which are among the shortest bonds between a first-row transition metal and nitrogen, with an average bond length of 2.0 Å.

**Magnetic Moments.** In addition to the optimized geometries, we also examined the magnetic moment on each metal in both the empty frameworks and gas-adsorbed complexes. Over 80% of the complexes (including all complexes of the type  $M_3(\text{btc})_2$ ) optimized to a magnetic moment of 2.0  $\mu_B$  or less per metal atom. The complexes with larger magnetic moments on the metal atoms (up to 5.0  $\mu_B$  per metal atom) were V-, Cr-, Mn-, Fe-, and Co-containing MOFs of the type  $M_2(\text{dobdc})$ . For each MOF, the  $[\text{MOF} + \text{O}_2]$  and  $[\text{MOF} + \text{N}_2]$  complexes generally had the same magnetic moments as the parent framework. The magnetic moments do not correlate with predicted binding energies.

**3.2. DFT: Calculated Binding Energies.** Static binding energies provide a quantitative measure of the various MOF-gas bonding modes discussed above. Binding energies were negative (indicating a favorable bonding interaction) in all instances. See Tables 2–5 for calculated energies.

Among the 3d metals, favorable bonding interactions ranged from −354 to −21 kJ·mol<sup>-1</sup> for oxygen binding and from −188 to −7 kJ·mol<sup>-1</sup> for nitrogen binding. Binding energies were not found to be dependent on MOF structure type. With the exception of  $\text{Mo}_3(\text{btc})_2$ , the 4d metals have significantly stronger binding energies than their 3d counterparts. Compared to the 3d elements in the same group, 4d transition metals studied here have greater electronegativity, resulting in stronger binding, regardless of geometry (side-on vs bent vs linear). This increased binding energy seen for 4d transition metals is greater for both nitrogen and oxygen, resulting in only modest  $\Delta\Delta E$ s for the 4d transition metals. The electro-

negativity of the metal is a less important factor than the occupancy of the metal d-orbitals, as evidenced by the fact that there is no correlation seen between binding energy and electronegativity within the 3d transition metals.

For both nitrogen and oxygen binding, the strongest interaction was with  $\text{Be}_3(\text{btc})_2$  (−424 and −421 kJ·mol<sup>-1</sup>, respectively), a particularly interesting result since neither nitrogen nor oxygen are bound to beryllium in the optimized structures. In contrast, neither oxygen nor nitrogen binds strongly to  $\text{Be}_2(\text{dobdc})$ ; calculations produced moderate energies of −14 and −15 kJ·mol<sup>-1</sup>, respectively. Examining the optimized  $[\text{Be}_3(\text{btc})_2 + \text{O}_2]$  and  $[\text{Be}_3(\text{btc})_2 + \text{N}_2]$  structures provides an obvious reason for these very strong binding energies. For the empty framework  $\text{Be}_3(\text{btc})_2$ , the beryllium atoms are constrained in a four-coordinate planar structure, which is a very strained geometry for second-row beryllium to adopt. Thus, the empty framework  $\text{Be}_3(\text{btc})_2$  is a particularly strained, high-energy structure. The addition of either oxygen or nitrogen to  $\text{Be}_3(\text{btc})_2$  allows the framework to twist such that the O–Be–O angles range from 92–153°, relieving the strain around the beryllium atom and resulting in a significantly lower energy structure. In contrast, the beryllium atom in  $\text{Be}_2(\text{dobdc})$  is in a tetrahedral configuration with the beryllium atom relatively inaccessible to the gas molecules and not under any excess strain; adding a gas molecule does not significantly change the geometry or energy of the framework. This finding is consistent with Koh and co-workers' report that carbon dioxide binds more strongly with  $\text{Be}_3(\text{btc})_2$  than with  $\text{Be}_2(\text{dobdc})$ ; this difference in binding energy was attributed to the fact that the beryllium atoms in  $\text{Be}_2(\text{dobdc})$  are relatively inaccessible to guest atoms.<sup>49</sup>

Other notably favorable bonding interactions occurred for oxygen to  $\text{Ti}_2(\text{dobdc})$  (−354 kJ·mol<sup>-1</sup>),  $\text{Ti}_3(\text{btc})_2$  (−329 kJ·mol<sup>-1</sup>),  $\text{Sc}_3(\text{btc})_2$  (−328 kJ·mol<sup>-1</sup>),  $\text{Mo}_2(\text{dobdc})$  (−267 kJ·mol<sup>-1</sup>),  $\text{Mn}_3(\text{btc})_2$  (−264 kJ·mol<sup>-1</sup>),  $\text{V}_2(\text{dobdc})$  (−264 kJ·mol<sup>-1</sup>),  $\text{Mg}_3(\text{btc})_2$  (−218 kJ·mol<sup>-1</sup>), and  $\text{Sc}_2(\text{dobdc})$  (−215 kJ·mol<sup>-1</sup>); and for nitrogen to  $\text{Mg}_3(\text{btc})_2$  (−228 kJ·mol<sup>-1</sup>). With only one exception (nitrogen binding to  $\text{Mg}_3(\text{btc})_2$ ), all of these very favorable bonding interactions are for oxygen



bonding to early transition metal MOFs. This is consistent with the trend mentioned above that early transition metals are more likely to bind oxygen in a side-on bonding mode and that side-on bonding is significantly stronger than bent or linear bonding.

**3.3. DFT: Difference in Binding Energies for Oxygen/Nitrogen Separations.** To achieve adequate separation of oxygen from nitrogen, it is necessary to identify MOFs with significantly stronger oxygen binding than nitrogen binding. We therefore use the difference in binding energies,  $\Delta\Delta E = -(\Delta E_{O_2} - \Delta E_{N_2})$ , to quantify this effect in the MOFs studied here (Table 6). A positive difference in binding energies  $\Delta\Delta E$

**Table 6.**  $\Delta\Delta E$ , Difference in Binding Energies between Oxygen and Nitrogen Binding, for Variants of  $M_3(btc)_2$  and  $M_2(dobdc)$

metal (M)	$\Delta\Delta E,^a$ (kJ·mol <sup>-1</sup> ) $M_3(btc)_2$ variant	$\Delta\Delta E,^a$ (kJ·mol <sup>-1</sup> ) $M_2(dobdc)$ variant
First-Row Transition Metals		
Sc	281	172
Ti	303	275
V	148	174
Cr	48	137
Mn	76	90
Fe	33	80
Co	19	41
Ni	9	34
Cu	3	2
Zn	-15	0
Second-Row Transition Metals		
Mo	5	139
Ru	50	26
Alkaline Earth Metals		
Be	-3	-1
Mg	-11	3

<sup>a</sup> $\Delta\Delta E$  calculated as  $-(\Delta E_{O_2} - \Delta E_{N_2})$ . In this convention, positive  $\Delta\Delta E$  indicates that binding to oxygen is stronger than binding to nitrogen.

indicates that the MOF has greater oxygen binding energy than nitrogen binding energy. Almost all MOFs examined had positive  $\Delta\Delta E$ s. MOFs with the greatest  $\Delta\Delta E$  are early transition metal MOFs, of both  $M_3(btc)_2$  and  $M_2(dobdc)$  types. Late transition metals and alkaline earth metals generally bind oxygen and nitrogen equally well, making them less suitable candidates for oxygen/nitrogen separation.

Binding energies ( $\Delta E_{gas}$ ) and the difference in binding energies ( $\Delta\Delta E$ ) are plotted together for the first row transition metal MOFs in Figure 6. For a given metal, both the binding energies and the difference in binding energies are provided for nitrogen and oxygen for each of the two MOF series studied. Using chromium as an example, Figure 6 shows that oxygen binding with  $Cr_2(dobdc)$  is the most energetically favorable, with a binding energy of  $-147$  kJ·mol<sup>-1</sup> (filled purple circle).  $Cr_3(btc)_2$  also binds oxygen strongly ( $-100$  kJ·mol<sup>-1</sup>, filled orange circle). Nitrogen binding to  $Cr_3(btc)_2$  and  $Cr_2(dobdc)$  are less favorable, with binding energies of  $-52$  kJ·mol<sup>-1</sup> (open orange circle) and  $-10$  kJ·mol<sup>-1</sup> (open purple circle), respectively. The difference in binding energies can be calculated for each MOF: for  $Cr_3(btc)_2$ , the difference in binding energies is  $48$  kJ·mol<sup>-1</sup> (orange bar) and the difference in binding energies for  $Cr_2(dobdc)$  is  $137$  kJ·mol<sup>-1</sup> (purple bar).

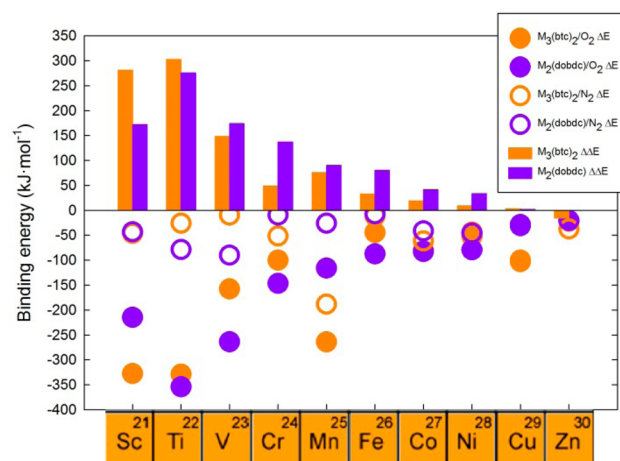


**Figure 6.** Difference in binding energies ( $\Delta\Delta E$ ) between oxygen and nitrogen binding (bars) and binding energies for nitrogen (open circles) and oxygen (closed circles), for variants of  $M_3(btc)_2$  (orange) and  $M_2(dobdc)$  (purple) containing first-row transition metals.

The data reveal several distinct trends for the first row transition metals in the two MOF series studied (see Figure 6). First, the differences in binding energies ( $\Delta\Delta E$ ) for a given metal are very similar across the two MOF structural types. Despite the striking differences in the  $M_3(btc)_2$  and  $M_2(dobdc)$  structure types, it is the type of metal rather than the MOF structure type (e.g., dimetal paddlewheel clusters vs infinite metal chains, void spaces of cages and windows vs long pores) that determines how effectively a MOF can separate oxygen from nitrogen. This is best illustrated by looking at the titanium and copper cases. The two titanium-containing MOFs are able to selectively bind oxygen over nitrogen equally well, and both MOFs show very large  $\Delta\Delta E$  values. The two copper-containing MOFs, on the other hand, have only modest oxygen and nitrogen binding energies. Although  $Cu_3(btc)_2$  binds both gases more strongly than  $Cu_2(dobdc)$  does, the differences in binding energy ( $\Delta\Delta E$ ) are almost identical for the two MOFs and much smaller than the titanium MOF  $\Delta\Delta E$ s. It would be enlightening to calculate oxygen and nitrogen binding energies for bare metal cations to see if this trend holds in the absence of the framework, but reference calculations on a simple  $M \cdots O_2$  system will miss many of the important interactions found in a MOF, including local coordination and spin state.

Second,  $\Delta E_{O_2}$  values (Figure 6, filled circles) are much stronger for early transition metals than for late transition metals. As the data indicate, MOFs containing early transition metals are able to bind oxygen in a side-on bonding mode, accounting for the greater binding energy for these MOFs. The  $\Delta E_{O_2}$  values follow the same trend seen by Koh and co-workers<sup>49</sup> for carbon dioxide binding energies. Although the carbon dioxide binding energies are more moderate than oxygen binding energies, they are greater for early transition metal MOFs ( $M_2(dobdc)$  and  $M_3(btc)_2$ ,  $M = Sc, Ti, V$ ) than late transition metal MOFs. In contrast,  $\Delta E_{N_2}$  values (Figure 6, open circles) are moderate (generally less than  $100$  kJ·mol<sup>-1</sup>) across all the 3d transition metal MOFs.

Taking the above trends into account,  $\Delta\Delta E$  values are much greater for early transition metal MOFs than for late transition metal MOFs. This large difference in binding energy for early transition metals is due to the strong oxygen binding exhibited by these MOFs.

**3.4. Comparison between Simulation and Experiment.** To validate the calculated binding energies, oxygen and nitrogen gas uptake experiments were performed for three MOFs:  $\text{Cu}_3(\text{btc})_2$ ,  $\text{Ni}_2(\text{dobdc})$ , and  $\text{Co}_2(\text{dobdc})$ . Low-temperature, low-pressure gas uptake measurements were chosen because they best represent the simulation conditions. Under these conditions ( $0.015 P/P_0$  at 77 K),  $\text{Cu}_3(\text{btc})_2$  adsorbed the most gas,  $25.8 \text{ mmol}\cdot\text{g}^{-1}$  of oxygen and  $22.5 \text{ mmol}\cdot\text{g}^{-1}$  of nitrogen.  $\text{Co}_2(\text{dobdc})$  and  $\text{Ni}_2(\text{dobdc})$  had very similar oxygen ( $18.0$  and  $15.0 \text{ mmol}\cdot\text{g}^{-1}$ , respectively) and nitrogen ( $13.8$  and  $12.0 \text{ mmol}\cdot\text{g}^{-1}$ , respectively) uptake. Each MOF had greater uptake of oxygen than nitrogen, which is qualitatively consistent with the generally stronger oxygen versus nitrogen binding energy seen in the simulations.

In order to determine whether binding energy is a good quantitative predictor of gas adsorption, the simulated binding energies were compared with gas adsorption at low temperature (Figure 7). To account for the fact that the binding energies are

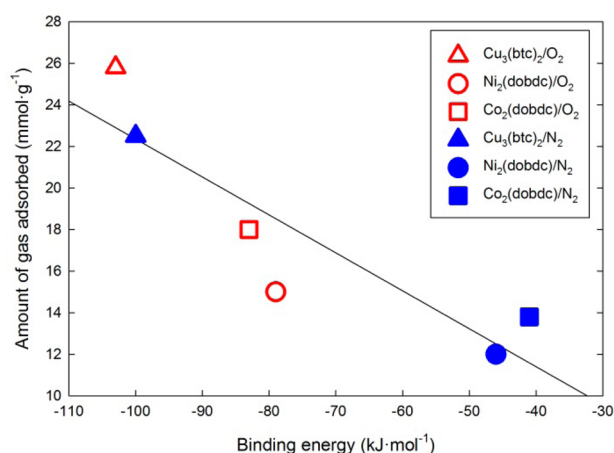


**Figure 7.** Correlation between experimental gas uptake ( $0.015 P/P_0$ ) at 77 K and simulated binding energy for oxygen (open red symbols) and nitrogen (filled blue symbols), for  $\text{Cu}_3(\text{btc})_2$  (triangles),  $\text{Ni}_2(\text{dobdc})$  (circles), and  $\text{Co}_2(\text{dobdc})$  (squares).

representative of the interaction between gas and the coordinatively unsaturated metal sites only, we measured gas uptake at very low pressure ( $0.015 P/P_0$ ). The combination of low temperature and strong adsorption (likely at multiple sites) of both oxygen and nitrogen in the MOFs studied resulted in near saturation of the frameworks at this low pressure. Despite this, good qualitative correlation was found between the experimental low-pressure, low-temperature gas uptake and simulated binding energy, for both nitrogen and oxygen. We note that there is a difference in behavior of the two framework types. For the  $\text{M}_2(\text{dobdc})$  frameworks, oxygen has a significantly stronger binding energy but only moderately larger gas uptake relative to nitrogen. The  $\text{Cu}_3(\text{btc})_2$  framework shows a different relationship between binding energy and gas adsorption: a relatively small difference in binding energies is associated with a moderate increase in gas uptake between nitrogen and oxygen. We attribute this to the presence of a second strong binding site in the  $\text{Cu}_3(\text{btc})_2$  framework, namely, the small octahedral cages.<sup>37,86</sup> Interaction energy between the gas molecules and small octahedral cages was not accounted for in the simulations, but is occurring experimentally.

Finally, to assess whether the difference in binding energies is a good predictor of selectivity, DFT  $\Delta\Delta E$  values were plotted

against the observed selectivity for oxygen over nitrogen, calculated as the ratio of oxygen to nitrogen amount adsorbed at 77 K,  $0.015 P/P_0$  (Figure 8). Good correlation is observed,

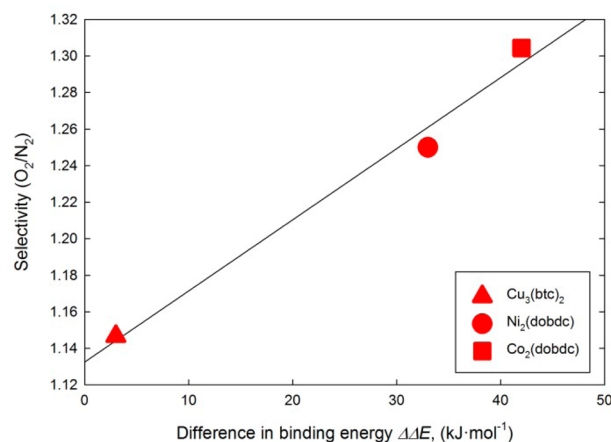


**Figure 8.** Correlation between experimental adsorption selectivity and simulated difference in binding energy for  $\text{Cu}_3(\text{btc})_2$  (triangles),  $\text{Ni}_2(\text{dobdc})$  (circles), and  $\text{Co}_2(\text{dobdc})$  (squares).

suggesting that the difference in binding energies can be used as a screening tool to identify MOFs that will be selective for oxygen over nitrogen.

Additionally, the difference in binding energies was compared to previously reported  $\text{O}_2/\text{N}_2$  selectivities, as reported by Bloch and co-workers<sup>7</sup> and Murray and co-workers<sup>51</sup> for  $\text{Fe}_2(\text{dobdc})$  and  $\text{Cr}_3(\text{btc})_2$ , respectively. Both MOFs are reported as having exceptionally strong selectivity for binding oxygen over nitrogen at room temperature, relative to other known MOFs. The differences in binding energies ( $\Delta\Delta E$ ) calculated here are both moderately large (80 and 48  $\text{kJ}\cdot\text{mol}^{-1}$ , respectively) and are significantly greater than the  $\Delta\Delta E$  for the extensively studied  $\text{Cu}_3(\text{btc})_2$  (3  $\text{kJ}\cdot\text{mol}^{-1}$ ). Although several MOFs examined here have calculated  $\Delta\Delta E$  values greater than those of  $\text{Fe}_2(\text{dobdc})$  and  $\text{Cr}_3(\text{btc})_2$ , those other early transition-metal MOFs are not known and could be synthetically challenging to prepare.

## 4. CONCLUSIONS

Dispersion-corrected DFT methods were used to estimate the binding energies of molecular oxygen and molecular nitrogen in 28 different MOFs, of the type  $\text{M}_3(\text{btc})_2$  and  $\text{M}_2(\text{dobdc})$ . A total of 14 variants of each MOF structural type were examined, differing only by the MOF metal (10 first-row transition metals, 2 second-row transition metals, and 2 alkaline earth metals). The calculated binding energies were validated by qualitative comparison with experimental gas adsorption measurements on three MOFs, namely,  $\text{Cu}_3(\text{btc})_2$ ,  $\text{Co}_2(\text{dobdc})$ ,  $\text{Ni}_2(\text{dobdc})$ , and recently with  $\text{M}-\text{Cu}_3(\text{btc})_2$  variations.<sup>87</sup>

The first-row transition metal results show a clear pattern for strong oxygen binding in MOFs with early transition metals (which have unfilled d-orbitals), regardless of the MOF structural type ( $\text{M}_3(\text{btc})_2$  vs  $\text{M}_2(\text{dobdc})$ ). These early transition-metal MOFs bind oxygen with a side-on bonding geometry associated with lengthening of the O–O bond and significant deformation around the binding site.

Nitrogen binding energies were moderate across the transition metal series and nitrogen binding geometry showed

no clear trend, although most  $[\text{MOF} + \text{N}_2]$  complexes optimized to a linear bonding mode.

With very large oxygen binding energies and only moderate nitrogen binding energies, early transition metals show the greatest difference in binding energies,  $\Delta\Delta E$ , suggesting that MOFs with early transition metals will be more effective at separating oxygen from nitrogen in an industrial setting. Specifically,  $\text{Sc}_3(\text{btc})_2$ ,  $\text{Ti}_3(\text{btc})_2$ ,  $\text{V}_3(\text{btc})_2$ ,  $\text{Sc}_2(\text{dobdc})$ ,  $\text{Ti}_2(\text{dobdc})$ ,  $\text{V}_2(\text{dobdc})$ ,  $\text{Cr}_2(\text{dobdc})$ , and  $\text{Mo}_2(\text{dobdc})$  stand out as strong candidates for oxygen/nitrogen separation, if they are synthetically viable.

The effect of temperature on gas adsorption will likely play a key role in the identification of candidate MOFs for gas separation related to oxyfuel combustion. While some MOFs show promise for selective binding of oxygen over nitrogen at room temperature, the reversibility of this process appears to be temperature dependent for some MOFs.<sup>7,51</sup> Future work will use DFT-based molecular dynamics simulations to examine the effect of temperature on oxygen and nitrogen binding by MOFs.

## ■ ASSOCIATED CONTENT

### ■ Supporting Information

Lattice parameters for optimized geometries of MOFs; oxygen and nitrogen adsorption isotherms measured at 77 K; calculated vs experimental before and after sorption XRD pattern for  $\text{Cu}_3(\text{btc})_2$ ,  $\text{Co}_2(\text{dobdc})$ , and  $\text{Ni}_2(\text{dobdc})$ . This material is available free of charge via the Internet at <http://pubs.acs.org>.

## ■ AUTHOR INFORMATION

### Corresponding Authors

\*E-mail: [jagreat@sandia.gov](mailto:jagreat@sandia.gov).

\*E-mail: [tmnenof@sandia.gov](mailto:tmnenof@sandia.gov).

### Notes

The authors declare no competing financial interest.

## ■ ACKNOWLEDGMENTS

Sandia National Laboratories is a multiprogram laboratory managed and operated by Sandia Corporation, a wholly owned subsidiary of Lockheed Martin Corporation, for the U.S. Department of Energy's National Nuclear Security Administration under Contract DE-AC04-94AL85000. This research was funded by Sandia's Laboratory Directed Research and Development program.

## ■ REFERENCES

- (1) Chai, S. W.; Kothare, M. V.; Sircar, S. Rapid Pressure Swing Adsorption for Reduction of Bed Size Factor of a Medical Oxygen Concentrator. *Ind. Eng. Chem. Res.* **2011**, *50*, 8703–8710.
- (2) Beaman, J. J. A Dynamic Model of a Pressure Swing Oxygen Generation System. *J. Dyn. Syst. Meas. Control* **1985**, *107*, 111–116.
- (3) Miller, R. L.; Ikels, K. G.; Lamb, M. J.; Boscola, E. J.; Ferguson, R. H. Molecular Sieve Generation of Aviator's Oxygen: Performance of a Prototype System Under Simulated Flight Conditions. *Aviat. Space Environ. Med.* **1980**, *51*, 665–673.
- (4) Manatt, S. A. Onboard Oxygen Generation Systems. *Aviat. Space Environ. Med.* **1981**, *52*, 645–653.
- (5) Jin, X.; Makel, A.; Farooq, S. Production of Argon from an Oxygen–Argon Mixture by Pressure Swing Adsorption. *Ind. Eng. Chem. Res.* **2006**, *45*, 5775–5787.
- (6) Sumida, K.; Rogow, D. L.; Mason, J. A.; McDonald, T. M.; Bloch, E. D.; Herm, Z. R.; Bae, T.-H.; Long, J. R. Carbon Dioxide Capture in Metal–Organic Frameworks. *Chem. Rev.* **2012**, *112*, 724–781.
- (7) Bloch, E. D.; Murray, L. J.; Queen, W. L.; Chavan, S.; Maximoff, S. N.; Bigi, J. P.; Krishna, R.; Peterson, V. K.; Grandjean, F.; Long, G. J.; et al. Selective Binding of  $\text{O}_2$  over  $\text{N}_2$  in a Redox-Active Metal–Organic Framework with Open Iron(II) Coordination Sites. *J. Am. Chem. Soc.* **2011**, *133*, 14814–14822.
- (8) Rodewald, A.; Kather, A.; Frie, S. Thermodynamic and Economic Aspects of the Hard Coal Based Oxyfuel Cycle. *Int. J. Green Energy* **2005**, *2*, 181–192.
- (9) Hu, Y.  $\text{CO}_2$  Capture from Oxy-Fuel Combustion Power Plants. *Licentiate Thesis*, KTH Royal Institute of Technology, Stockholm, Sweden, 2011.
- (10) Castle, W. F. Air Separation and Liquefaction: Recent Developments and Prospects for the Beginning of the New Millennium. *Int. J. Refrig.* **2002**, *25*, 158–172.
- (11) Li, J.-R.; Ma, Y.; McCarthy, M. C.; Sculley, J.; Yu, J.; Jeong, H.-K.; Balbuena, P. B.; Zhou, H.-C. Carbon Dioxide Capture-Related Gas Adsorption and Separation in Metal–Organic Frameworks. *Coord. Chem. Rev.* **2011**, *255*, 1791–1823.
- (12) Carta, M.; Malpass-Evans, R.; Croad, M.; Rogan, Y.; Jansen, J. C.; Bernardo, P.; Bazzarelli, F.; McKeown, N. B. An Efficient Polymer Molecular Sieve for Membrane Gas Separations. *Science* **2013**, *339*, 303–307.
- (13) Hutson, N. D.; Rege, S. U.; Yang, R. T. Mixed Cation Zeolites:  $\text{Li}_x\text{Ag}_{1-x}\text{X}$  as a Superior Adsorbent for Air Separation. *AIChE J.* **1999**, *45*, 724–734.
- (14) Reid, C. R.; Thomas, K. M. Adsorption of Gases on a Carbon Molecular Sieve Used for Air Separation: Linear Adsorptives as Probes for Kinetic Selectivity. *Langmuir* **1999**, *15*, 3206–3218.
- (15) Nandi, S. P.; Walker, P. L., Jr. Separation of Oxygen and Nitrogen Using 5Å Zeolite and Carbon Molecular Sieves. *Sep. Sci.* **1976**, *11*, 441–453.
- (16) Sircar, S.; Myers, A. L., Gas Separation by Zeolites. In *Handbook of Zeolite Science and Technology*; Auerbach, S. M., Carrado, K. A., Dutta, P. K., Eds.; Marcel Dekker, Inc: New York, 2003; p 1184.
- (17) Kreno, L. E.; Leong, K.; Farha, O. K.; Allendorf, M. D.; Van Duyn, R. P.; Hupp, J. T. Metal–Organic Framework Materials as Chemical Sensors. *Chem. Rev.* **2012**, *112*, 1105–1125.
- (18) Zeitler, T. R.; Van Heest, T.; Sholl, D. S.; Allendorf, M. D.; Greathouse, J. A. Predicting Low-Pressure  $\text{O}_2$  Adsorption in Nanoporous Framework Materials for Sensing Applications. *Chem-PhysChem* **2013**, *14*, 3740–3750.
- (19) Buso, D.; Jasieniak, J.; Lay, M. D. H.; Schiavuta, P.; Scopece, P.; Laird, J.; Amenitsch, H.; Hill, A. J.; Falcaro, P. Highly Luminescent Metal–Organic Frameworks Through Quantum Dot Doping. *Small* **2012**, *8*, 80–88.
- (20) Sava, D. F.; Rohwer, L. E. S.; Rodriguez, M. A.; Nenoff, T. M. Intrinsic Broad-Band White-Light Emission by a Tuned, Corrugated Metal–Organic Framework. *J. Am. Chem. Soc.* **2012**, *134*, 3983–3986.
- (21) Perry, J. J., IV; Feng, P. L.; Meek, S. T.; Leong, K.; Doty, F. P.; Allendorf, M. D. Connecting Structure with Function in Metal–Organic Frameworks to Design Novel Photo- and Radioluminescent Materials. *J. Mater. Chem.* **2012**, *22*, 10235–10248.
- (22) Lee, J.; Farha, O. K.; Roberts, J.; Scheidt, K. A.; Nguyen, S. T.; Hupp, J. T. Metal–Organic Framework Materials as Catalysts. *Chem. Soc. Rev.* **2009**, *38*, 1450–1459.
- (23) Corma, A.; García, H.; Llabrés i Xamena, F. X. Engineering Metal Organic Frameworks for Heterogeneous Catalysis. *Chem. Rev.* **2010**, *110*, 4606–4655.
- (24) Sava, D. F.; Chapman, K. W.; Rodriguez, M. A.; Greathouse, J. A.; Crozier, P. S.; Zhao, H.; Chupas, P. J.; Nenoff, T. M. Competitive  $\text{I}_2$  Sorption by Cu-BTC from Humid Gas Streams. *Chem. Mater.* **2013**, *25*, 2591–2596.
- (25) Sava, D. F.; Rodriguez, M. A.; Chapman, K. W.; Chupas, P. J.; Greathouse, J. A.; Crozier, P. S.; Nenoff, T. M. Capture of Volatile Iodine, a Gaseous Fission Product, by Zeolitic Imidazolate Framework-8. *J. Am. Chem. Soc.* **2011**, *133*, 12398–12401.
- (26) Horcajada, P.; Chalati, T.; Serre, C.; Gillet, B.; Sebrie, C.; Baati, T.; Eubank, J. F.; Heurtaux, D.; Clayette, P.; Kreuz, C.; et al. Porous



Metal–Organic Framework Nanoscale Carriers as a Potential Platform for Drug Delivery and Imaging. *Nat. Mater.* **2010**, *9*, 172–178.

(27) Huxford, R. C.; Della Rocca, J.; Lin, W. Metal–Organic Frameworks as Potential Drug Carriers. *Curr. Opin. Chem. Biol.* **2010**, *14*, 262–268.

(28) Fernandez, M.; Trefiak, N. R.; Woo, T. K. Atomic Property Weighted Radial Distribution Functions Descriptors of Metal–Organic Frameworks for the Prediction of Gas Uptake Capacity. *J. Phys. Chem. C* **2013**, *117*, 14095–14105.

(29) Suh, M. P.; Park, H. J.; Prasad, T. K.; Lim, D.-W. Hydrogen Storage in Metal–Organic Frameworks. *Chem. Rev.* **2012**, *112*, 782–835.

(30) Zang, J.; Nair, S.; Sholl, D. S. Prediction of Water Adsorption in Copper-Based Metal–Organic Frameworks Using Force Fields Derived from Dispersion-Corrected DFT Calculations. *J. Phys. Chem. C* **2013**, *117*, 7519–7525.

(31) Lim, W.-X.; Thornton, A. W.; Hill, A. J.; Cox, B. J.; Hill, J. M.; Hill, M. R. High Performance Hydrogen Storage from Be-BTB Metal–Organic Framework at Room Temperature. *Langmuir* **2013**, *29*, 8524–8533.

(32) Yang, G.; Santana, J. A.; Rivera-Ramos, M. E.; García-Ricard, O.; Saavedra-Arias, J. J.; Ishikawa, Y.; Hernández-Maldonado, A. J.; Raptis, R. G. A Combined Experimental and Theoretical Study of Gas Sorption on Nanoporous Silver Triazolato Metal–Organic Frameworks. *Microporous Mesoporous Mater.* **2014**, *183*, 62–68.

(33) Li, T.; Rosi, N. L. Screening and Evaluating Aminated Cationic Functional Moieties for Potential CO<sub>2</sub> Capture Applications Using an Anionic MOF Scaffold. *Chem. Commun.* **2013**, *49*, 11385–11387.

(34) Yang, Q.; Liu, D.; Zhong, C.; Li, J.-R. Development of Computational Methodologies for Metal–Organic Frameworks and Their Application in Gas Separations. *Chem. Rev.* **2013**, *113*, 8261–8323.

(35) Bae, Y.-S.; Mulfort, K. L.; Frost, H.; Ryan, P.; Punnathanam, S.; Broadbelt, L. J.; Hupp, J. T.; Snurr, R. Q. Separation of CO<sub>2</sub> from CH<sub>4</sub> Using Mixed-Ligand Metal–Organic Frameworks. *Langmuir* **2008**, *24*, 8592–8598.

(36) Li, J.-R.; Sculley, J.; Zhou, H.-C. Metal–Organic Frameworks for Separations. *Chem. Rev.* **2012**, *112*, 869–932.

(37) Parkes, M. V.; Staiger, C. L.; Perry, J. J., IV; Allendorf, M. D.; Greathouse, J. A. Screening Metal–Organic Frameworks for Selective Noble Gas Adsorption in Air: Effect of Pore Size and Framework Topology. *Phys. Chem. Chem. Phys.* **2013**, *15*, 9093–9106.

(38) Böhme, U.; Barth, B.; Paula, C.; Kuhnt, A.; Schwieger, W.; Mundstock, A.; Caro, J.; Hartmann, M. Ethene/Ethane and Propene/Propane Separation via the Olefin and Paraffin Selective Metal–Organic Framework Adsorbents CPO-27 and ZIF-8. *Langmuir* **2013**, *29*, 8592–8600.

(39) Demir, B.; Ahunbay, M. G. CO<sub>2</sub>/CH<sub>4</sub> Separation in Ion-Exchanged Zeolite-Like Metal Organic Frameworks with Sodalite Topology (sod-ZMOFs). *J. Phys. Chem. C* **2013**, *117*, 15647–15658.

(40) Duan, X.; Cai, J.; Yu, J.; Wu, C.; Cui, Y.; Yang, Y.; Qian, G. Three-Dimensional Copper (II) Metal–Organic Framework with Open Metal Sites and Anthracene Nucleus for Highly Selective C<sub>2</sub>H<sub>2</sub>/CH<sub>4</sub> and C<sub>2</sub>H<sub>2</sub>/CO<sub>2</sub> Gas Separation at Room Temperature. *Microporous Mesoporous Mater.* **2013**, *181*, 99–104.

(41) Bozbiyik, B.; Duerinck, T.; Lannoeye, J.; De Vos, D. E.; Baron, G. V.; Denayer, J. F. M. Adsorption and Separation of *n*-Hexane and Cyclohexane on the UiO-66 Metal–Organic Framework. *Microporous Mesoporous Mater.* **2014**, *183*, 143–149.

(42) Farha, O. K.; Hupp, J. T. Rational Design, Synthesis, Purification, and Activation of Metal–Organic Framework Materials. *Acc. Chem. Res.* **2010**, *43*, 1166–1175.

(43) Stock, N.; Biswas, S. Synthesis of Metal–Organic Frameworks (MOFs): Routes to Various MOF Topologies, Morphologies, and Composites. *Chem. Rev.* **2012**, *112*, 933–969.

(44) Sikora, B. J.; Wilmer, C. E.; Greenfield, M. L.; Snurr, R. Q. Thermodynamic Analysis of Xe/Kr Selectivity in Over 137000 Hypothetical Metal–Organic Frameworks. *Chem. Sci.* **2012**, *3*, 2217–2223.

(45) Wilmer, C. E.; Leaf, M.; Lee, C. Y.; Farha, O. K.; Hauser, B. G.; Hupp, J. T.; Snurr, R. Q. Large-Scale Screening of Hypothetical Metal–Organic Frameworks. *Nat. Chem.* **2011**, *4*, 83–89.

(46) Van Heest, T. M.; Teich-McGoldrick, S. L.; Greathouse, J. A.; Allendorf, M. D.; Sholl, D. S. Identification of Metal–Organic Framework Materials for Adsorption Separation of Rare Gases: Applicability of Ideal Adsorbed Solution Theory (IAST) and Effects of Inaccessible Framework Regions. *J. Phys. Chem. C* **2012**, *116*, 13183–13195.

(47) Watanabe, T.; Sholl, D. S. Accelerating Applications of Metal–Organic Frameworks for Gas Adsorption and Separation by Computational Screening of Materials. *Langmuir* **2012**, *28*, 14114–14128.

(48) Wilmer, C. E.; Farha, O. K.; Bae, Y.-S.; Hupp, J. T.; Snurr, R. Q. Structure-Property Relationships of Porous Materials for Carbon Dioxide Separation and Capture. *Energy Environ. Sci.* **2012**, *5*, 9849–9856.

(49) Koh, H. S.; Rana, M. K.; Hwang, J.; Siegel, D. J. Thermodynamic Screening of Metal-Substituted MOFs for Carbon Capture. *Phys. Chem. Chem. Phys.* **2013**, *15*, 4573–4581.

(50) Southon, P. D.; Price, D. J.; Nielsen, P. K.; McKenzie, C. J.; Kepert, C. J. Reversible and Selective O<sub>2</sub> Chemisorption in a Porous Metal–Organic Host Material. *J. Am. Chem. Soc.* **2011**, *133*, 10885–10891.

(51) Murray, L. J.; Dinca, M.; Yano, J.; Chavan, S.; Bordiga, S.; Brown, C. M.; Long, J. R. Highly-Selective and Reversible O<sub>2</sub> Binding in Cr<sub>3</sub>(1,3,5-benzenetricarboxylate)<sub>2</sub>. *J. Am. Chem. Soc.* **2010**, *132*, 7856–7857.

(52) Bae, Y.-S.; Spokoyny, A. M.; Farha, O. K.; Snurr, R. Q.; Hupp, J. T.; Mirkin, C. A. Separation of Gas Mixtures Using Co(II) Carborane-Based Porous Coordination Polymers. *Chem. Commun.* **2010**, *46*, 3478–3480.

(53) Li, Y.; Yang, R. T. Gas Adsorption and Storage in Metal–Organic Framework MOF-177. *Langmuir* **2007**, *23*, 12937–12944.

(54) Mu, B.; Schoenecker, P. M.; Walton, K. S. Gas Adsorption Study on Mesoporous Metal–Organic Framework UMCM-1. *J. Phys. Chem. C* **2010**, *114*, 6464–6471.

(55) Xie, L.; Liu, S.; Gao, C.; Cao, R.; Cao, J.; Sun, C.; Su, Z. Mixed-Valence Iron(II, III) Trimesates with Open Frameworks Modulated by Solvents. *Inorg. Chem.* **2007**, *46*, 7782–7788.

(56) Chui, S. S.-Y.; Lo, S. M.-F.; Charmant, J. P. H.; Orpen, A. G.; Williams, I. D. A Chemically Functionalizable Nanoporous Material [Cu<sub>3</sub>(TMA)<sub>2</sub>(H<sub>2</sub>O)<sub>3</sub>]<sub>n</sub>. *Science* **1999**, *283*, 1148–1150.

(57) Bloch, E. D.; Queen, W. L.; Krishna, R.; Zdrozny, J. M.; Brown, C. M.; Long, J. R. Hydrocarbon Separations in a Metal–Organic Framework with Open Iron(II) Coordination Sites. *Science* **2012**, *335*, 1606–1610.

(58) Dietzel, P. D. C.; Morita, Y.; Blom, R.; Fjellvåg, H. An In Situ High-Temperature Single-Crystal Investigation of a Dehydrated Metal–Organic Framework Compound and Field-Induced Magnetization of One-Dimensional Metal–Oxygen Chains. *Angew. Chem., Int. Ed.* **2005**, *44*, 6354–6358.

(59) Dietzel, P. D. C.; Panella, B.; Hirscher, M.; Blom, R.; Fjellvåg, H. Hydrogen Adsorption in a Nickel Based Coordination Polymer with Open Metal Sites in the Cylindrical Cavities of the Desolvated Framework. *Chem. Commun.* **2006**, *2006*, 959–961.

(60) Dietzel, P. D. C.; Johnsen, R. E.; Blom, R.; Fjellvåg, H. Structural Changes and Coordinatively Unsaturated Metal Atoms on Dehydration of Honeycomb Analogous Microporous Metal–Organic Frameworks. *Chem.—Eur. J.* **2008**, *14*, 2389–2397.

(61) Dietzel, P. D. C.; Blom, R.; Fjellvåg, H. Base-Induced Formation of Two Magnesium Metal–Organic Framework Compounds with a Bifunctional Tetratopic Ligand. *Eur. J. Inorg. Chem.* **2008**, *2008*, 3624–3632.

(62) Rowsell, J. L. C.; Yaghi, O. M. Effects of Functionalization, Catenation, and Variation of the Metal Oxide and Organic Linking Units on the Low-Pressure Hydrogen Adsorption Properties of Metal–Organic Frameworks. *J. Am. Chem. Soc.* **2006**, *128*, 1304–1315.



- (63) Rosi, N. L.; Kim, J.; Eddaoudi, M.; Chen, B.; O'Keeffe, M.; Yaghi, O. M. Rod Packings and Metal-Organic Frameworks Constructed from Rod-Shaped Secondary Building Units. *J. Am. Chem. Soc.* **2005**, *127*, 1504–1518.
- (64) Yu, D.; Yazaydin, A. O.; Lane, J. R.; Dietzel, P. D. C.; Snurr, R. Q. A Combined Experimental and Quantum Chemical Study of CO<sub>2</sub> Adsorption in the Metal-Organic Framework CPO-27 with Different Metals. *Chem. Sci.* **2013**, *4*, 3544–3556.
- (65) Zhou, W.; Wu, H.; Yildirim, T. Enhanced H<sub>2</sub> Adsorption in Isostructural Metal-Organic Frameworks with Open Metal Sites: Strong Dependence of the Binding Strength on Metal Ions. *J. Am. Chem. Soc.* **2008**, *130*, 15268–15269.
- (66) Park, J.; Kim, H.; Han, S. S.; Jung, Y. Tuning Metal-Organic Frameworks with Open-Metal Sites and Its Origin for Enhancing CO<sub>2</sub> Affinity by Metal Substitution. *J. Phys. Chem. Lett.* **2012**, *3*, 826–829.
- (67) Rana, M. K.; Koh, H. S.; Hwang, J.; Siegel, D. J. Comparing van der Waals Density Functionals for CO<sub>2</sub> Adsorption in Metal Organic Frameworks. *J. Phys. Chem. C* **2012**, *116*, 16957–16968.
- (68) Dion, M.; Rydberg, H.; Schröder, E.; Langreth, D. C.; Lundqvist, B. I. Van der Waals Density Functional for General Geometries. *Phys. Rev. Lett.* **2004**, *92*, 246401.
- (69) Poloni, R.; Smit, B.; Neaton, J. B. CO<sub>2</sub> Capture by Metal-Organic Frameworks with van der Waals Density Functionals. *J. Phys. Chem. A* **2012**, *116*, 4957–4964.
- (70) Kresse, G.; Furthmüller, J. Efficient Iterative Schemes for *ab Initio* Total-Energy Calculations using a Plane-Wave Basis Set. *Phys. Rev. B: Condens. Matter Mater. Phys.* **1996**, *54*, 11169–11186.
- (71) Perdew, J. P.; Burke, K.; Ernzerhof, M. Generalized Gradient Approximation Made Simple. *Phys. Rev. Lett.* **1996**, *77*, 3865–3868.
- (72) Perdew, J. P.; Burke, K.; Ernzerhof, M. Errata: Generalized Gradient Approximation Made Simple. *Phys. Rev. Lett.* **1997**, *78*, 1396.
- (73) Grimme, S. Semiempirical GGA-Type Density Functional Constructed with a Long-Range Dispersion Correction. *J. Comput. Chem.* **2006**, *27*, 1787–1799.
- (74) Zhang, I. Y.; Xu, X. Doubly Hybrid Density Functional for Accurate Description of Thermochemistry, Thermochemical Kinetics and Nonbonded Interactions. *Int. Rev. Phys. Chem.* **2011**, *30*, 115–160.
- (75) Kresse, G.; Joubert, D. From Ultrasoft Pseudopotentials to the Projector Augmented-Wave Method. *Phys. Rev. B: Condens. Matter Mater. Phys.* **1999**, *59*, 1758–1775.
- (76) Blöchl, P. E. Projector Augmented-Wave Method. *Phys. Rev. B: Condens. Matter Mater. Phys.* **1994**, *50*, 17953–17979.
- (77) Watanabe, T.; Sholl, D. S. Molecular Chemisorption on Open Metal Sites in Cu<sub>3</sub>(benzenetricarboxylate)<sub>2</sub>: A Spatially Periodic Density Functional Theory Study. *J. Chem. Phys.* **2010**, *133*, 094509.
- (78) Ray, K. G.; Olmsted, D. L.; Houndonougbo, Y.; Laird, B. B.; Asta, M. Origins of CH<sub>4</sub>/CO<sub>2</sub> Adsorption Selectivity in Zeolitic Imidazolate Frameworks: A van der Waals Density Functional Study. *J. Phys. Chem. C* **2013**, *117*, 14642–14651.
- (79) Caskey, S. R.; Wong-Foy, A. G.; Matzger, A. J. Dramatic Tuning of Carbon Dioxide Uptake via Metal Substitution in a Coordination Polymer with Cylindrical Pores. *J. Am. Chem. Soc.* **2008**, *130*, 10870–10871.
- (80) He, Y.; Krishna, R.; Chen, B. Metal–Organic Frameworks with Potential for Energy-Efficient Adsorptive Separation of Light Hydrocarbons. *Energy Environ. Sci.* **2012**, *5*, 9107–9120.
- (81) Geier, S. J.; Mason, J. A.; Bloch, E. D.; Queen, W. L.; Hudson, M. R.; Brown, C. M.; Long, J. R. Selective Adsorption of Ethylene over Ethane and Propylene over Propane in the Metal-Organic Frameworks M<sub>2</sub>(dobdc) (M = Mg, Mn, Fe, Co, Ni, Zn). *Chem. Sci.* **2013**, *4*, 2054–2061.
- (82) Statistics obtained by searching for all structures with either M–O or M–N bonds (respectively) in the Cambridge Structural Database, version 5.35, as identified using the ConQuest and Mercury programs.
- (83) Allen, F. H. The Cambridge Structural Database: A Quarter of a Million Crystal Structures and Rising. *Acta Crystallogr., Sect. B: Struct. Sci.* **2002**, *58*, 380–388.
- (84) Bruno, I. J.; Cole, J. C.; Edgington, P. R.; Kessler, M.; Macrae, C. F.; McCabe, P.; Pearson, J.; Taylor, R. New Software for Searching the Cambridge Structural Database and Visualizing Crystal Structures. *Acta Crystallogr., Sect. B: Struct. Sci.* **2002**, *58*, 389–397.
- (85) Macrae, C. F.; Edgington, P. R.; McCabe, P.; Pidcock, E.; Shields, G. P.; Taylor, R.; Towler, M.; van de Streek, J. Mercury: Visualization and Analysis of Crystal Structures. *J. Appl. Crystallogr.* **2006**, *39*, 453–457.
- (86) García-Pérez, E.; Gascón, J.; Morales-Flórez, V.; Castillo, J. M.; Kapteijn, F.; Calero, S. Identification of Adsorption Sites in Cu-BTC by Experimentation and Molecular Simulation. *Langmuir* **2009**, *25*, 1725–1731.
- (87) Sava Gallis, D. F.; Parkes, M. V.; Greathouse, J. A.; Zhang, X.; Nenoff, T. M. Enhanced O<sub>2</sub> Selectivity versus N<sub>2</sub> by Partial Metal Substitution in Cu-BTC. *Chem. Mater.* **2015**, DOI: 10.1021/cm5042293, in process.